Supplementary Information for

Efficient and scalable perovskite solar cells achieved by buried interface engineering

Tao Wang[1,2,3], Liang Qiao[1,2,3], Tianshi Ye[1,2,3], Weiyu Kong[1,2,3], Fang Zeng[4], Yao Zhang[1], Ruitian Sun[1,2,3], Lin Zhang[1,2,3], Han Chen[1], Rongkun Zheng[4], Xudong Yang[1,2,3]*

[1]State Key Laboratory of Metal Matrix Composites, Shanghai Jiao Tong University, Shanghai 200240, China.

[2]Center of Hydrogen Science, School of Materials Science and Engineering, Shanghai Jiao Tong University, Shanghai 200240, China.

[3]Zhangjiang Institute for Advanced Study, Shanghai Jiao Tong University, Shanghai 201210, China.

[4]School of Physics, Sydney Nano Institute, The University of Sydney; Sydney NSW 2006, Australia.

* Corresponding author. Email: yang.xudong@sjtu.edu.cn (X.Y.)

Materials.

All the chemicals were used as received. The poly(triaryl amine) (PTAA) and the dopant 2,3,5,6-tetrafluoro-7,7,8,8-tetracyanoquinodimethane (F4TCNQ) were purchased from Xi'an Polymer Light Technology. Lead iodide (PbI_2, 99.99% trace metals basis), organic halide salts, and 1-ethyl-3-methylimidazolium tetrachloroferrate (III) (EMIM-$FeCl_4$) were purchased from Tokyo Chemical Industry (TCI). Lead bromide ($PbBr_2$, 99.999% trace metals basis), caesium iodide (CsI), and 1-ethyl-3-methylimidazolium tetrachloroaluminate (EMIM-$AlCl_4$) were purchased from Sigma Aldrich. Phenyl-C61butyric acid methyl ester (PCBM) and bathocuproine (BCP) were purchased from Luminescence technology corp. All the anhydrous solvents were purchased from Sigma-Aldrich.

Anion insertion methodology

The PTAA thin films were deposited on substrates by spin-coating PTAA solution dissolved in toluene (2 mg/ml or 20 mg/ml) and as-prepared films were annealed at 100 °C for 10 min. For the anion insertion process, the as-prepared PTAA film was immersed in a hot dopant solution at 60 °C for 2 min, and the residual dopants and by-products were washed off the surface using acetonitrile by spin coating. The substrates were annealed at 70 °C for 5 min. Dopant solutions were prepared by co-dissolving 5 mM F4TCNQ and 25 mM EMIM-$AlCl_4$ in acetonitrile and stirring at 60 °C for 0.5 h. In this process, the neutral PTAA was p-doped firstly with the initiator molecule F4TCNQ via a charge-transfer interaction: (i) PTAA+F4TCNQ→[$PTAA^{\bullet+}F4TCNQ^{\bullet-}$]. The $AlCl_4^-$ anions were inserted spontaneously into PTAA by exchanging with F4TCNQ radical anions driven by the gain of Gibbs free energy[1]: (ii) [$PTAA^{\bullet+}F4TCNQ^{\bullet-}$]+$EMIM^+AlCl_4^-$→[$PTAA^{\bullet+}AlCl_4^-$]+$EMIM^+$+$F4TCNQ^{\bullet-}$,
resulting in the formation of a solid-state donor-acceptor complex [$PTAA^{\bullet+}AlCl_4^-$] ($AlCl_4$-PTAA).

Perovskite film preparation and device fabrication.

Indium tin oxide (ITO)-coated substrates were etched with zinc powder and diluted

hydrochloric acid (HCl) to produce desired patterns. The patterned substrates were sequentially cleaned with soap, deionized water, ethanol, and acetone under ultrasonication, and then dried with dry nitrogen. Before use, the substrates were cleaned with ultraviolet ozone for 15 min and transferred to the N_2 glove box. PTAA solution (2 mg/mL dissolved in toluene) was spin-coated onto the ITO substrates at a speed of 6000 r.p.m. for 35 s, and then the films were annealed at 100 °C for 10 min. Subsequently, the as-prepared PTAA films are post-processing via an anion insertion process. The perovskite films were fabricated by the anti-solvent method. The 1.4 M $(CsPbI_3)_{0.05}[(FAPbI_3)_{0.92}(MAPbBr_3)_{0.08}]_{0.95}$ perovskite solution (DMF/DMSO = 4:1) was spin-coated at 2,000 r.p.m. for 10 s and 4000 r.p.m. for 30 s onto the ITO/PTAA substrates[2]. 20 seconds into the 4000 r.p.m. setting, 150 μL of ethyl acetate was poured on the center of the spinning substrates and the samples were heated at 100 °C for 30 min. After cooling to room temperature, 4 mM of phenethylammonium iodide solution dissolved in IPA was spin-coated onto the perovskite surface at 5,000 r.p.m. PCBM (20 mg/L in chlorobenzene) was spun onto the perovskite layer at a speed of 1000 r.p.m. 150 μl of BCP saturated solution in methanol was dropped onto the samples drop by drop at 5000 r.p.m. Finally, the samples were transferred to an evaporation chamber, and silver (80 nm) was deposited under a vacuum ($< 10^{-5}$ Pa).

PTAA film characterizations.

The electrical conductivity of pristine and anion-inserted PTAA films was measured using 2×1.5 cm patterned ITO-coated glass with one vertical etched line engraved by laser. The PTAA solution (20 mg/ml) in toluene was spin-coated on pre-patterned substrates at a spin speed of 3000 r.p.m. The width and length of the non-conducting channel were 100 μm and 1.5 cm, respectively. The thickness of the ITO was 180 nm. Current-Voltage (*I-V*) characteristics were measured using a multi-functional electrochemical analysis instrument (Zahner, Germany). Electrical conductivity was calculated as $\sigma = (L/Wd) \times (dV/dI)$, where L = 1.5 cm is the length of the channel, W = 100 μm is the width of the channel, and d = 180 nm is the thickness of the ITO.

Hole mobility of pristine and anion-inserted PTAA films was determined *vis* space-charge-limited current (SCLC) measurement on a hole-only device (ITO/30 nm MoO_3/PTAA/30 nm MoO_3/70nm Au). The MoO_3 and Au layers were all deposited by thermal evaporation. The PTAA thin films were deposited on substrates by spin-coating a PTAA solution (20 mg/ml) at 3000 r.p.m. and as-prepared films were annealed at 100 °C for 10 min. The classic Mott-Gurney equation was used to determine the mobility: $J = 9\mu\varepsilon_0\varepsilon_r V^2/(8d^3)$, where ε_r≈8.26 is the average dielectric constant of the blended film[3], ε_0 is the vacuum permittivity of the free space, μ is the hole mobility, V is the applied bias, and d is the film thickness.

UV-vis-NIR absorption spectra and transmittance spectra of pristine and anion-inserted PTAA samples were recorded by a Shimadzu UV 2450 spectrometry. Infrared absorption spectra were recorded with a Nicolet 6700 FTIR spectrometer (Thermo Fisher). Electron spin resonance (ESR) spectroscopy was analyzed by a Bruker EMX-8 spectrometer. Atomic force microscopy (AFM) and Kelvin Probe Force Microscopy (KPFM) were all recorded by a Bruker FastScan Bio instrument. Work function can be calculated using the following equation: $CPD = (\Phi_{sample} - \Phi_{tip})/e$. Φ_{sample} and $\Phi_{tip}$are the work function of the sample surface and Pt/Ir-coated tip, respectively. e is the elementary charge of an electron. Φ_{tip} is calibrated with Au (5.2 eV). The ultraviolet photoelectron spectroscopy (UPS) was measured by Thermo ESCALAB 250 with a non-monochromated He Iα photon source ($h\nu$ = 21.22 eV). The static contact angle with the water droplet was conducted on DSA 100 contact angle measuring device (KRUSS GmbH, Germany). Time-of-flight secondary ion mass spectrometry (ToF-SIMS) measurements were based on the focused ion beam ToF-SIMS spectrometer (ION TOF ToF SIMS 5-100).

Perovskite film characterizations.

UV-Vis absorption spectra of perovskite film samples were recorded by a Shimadzu UV 2450 spectrometry. Steady-state photoluminescence (PL) spectra and Time-

resolved photoluminescence (TRPL) spectra were obtained by FLS1000. The excitation wavelength was set as 520 nm. The ultraviolet photoelectron spectroscopy (UPS) was measured by Thermo ESCALAB 250 with a non-monochromated He Iα photon source ($h\nu$ = 21.22 eV). The XRD patterns were recorded on a Rigaku Ultima IV powder X-ray diffractometer using Cu Kα radiation. The SEM images were acquired using Field emission scanning electron microscopy (JSM-7800F).

Lift-off process and buried interface characterizations.

The sample preparation for the lift-off process was based on the previous literature[4]. Briefly, PTAA solution (30 mg/ml) in chlorobenzene was spin-coated onto the pre-cleaned ITO substrates at 4000 r.p.m. for 25 s and annealed at 100 °C for 15 min. The anions insertion process was carried out as mentioned before. Subsequently, the perovskite films were deposited onto the PTAA and $AlCl_4$-PTAA substrates, and then the samples were covered with the Cu electrode through thermal evaporation with a thickness of 300 nm. The as-prepared samples were immersed in CB solvent for 2-3 h until the perovskite films with Cu foils were detached from the ITO substrates, and the films were rinsed twice by CB. Finally, the integrated films were turned the bottom side up and transferred to the ITO substrates.

The confocal PL mapping images were carried out on a Leica TCS SP8 STED 3X system. The excitation wavelength was set as 470 nm and the detection range was 700-800 nm. XPS spectra for the bottom sides of the perovskite films were recorded by AXIS Ultra DLD (Kratos Analytical Ltd.). The trap density of perovskite films was determined by the space-charge-limited current (SCLC) method on the hole-only device with the architecture of ITO/PTAA/Perovskite/Spiro-OMeTAD/Ag. The trap-filled limit voltage (V_{TFL}) determined as the onset voltage of the TFL regime (n > 3) can be used to calculate N_{t} with the equation: $N_t = 2\varepsilon_0\varepsilon_r V_{TFL}/qL^2$, in which ε_0 is the vacuum permittivity, ε_{r} is the relative permittivity of perovskite, which can be taken as the value of 46.9 for $FAPbI_3$, and L is the thickness of the perovskite film[5].

Device characterizations.

Field emission scanning electron microscopy (TESCAN MAIA3 GMU model 2016) was used to observe the cross-sectional SEM image of the complete device. Current-Voltage (*I–V*) curves of the perovskite solar cells were measured with a digital source meter (Keithley 2400) under simulated solar illumination at AM1.5G (100 mW cm^{-2}). The light source was calibrated by a standard silicon reference cell (Wacom Denso Co., Japan). The measurement was conducted forward (from −0.2 to 1.2 V) scan. The step voltage and delay time were fixed at 10 mV and 200 ms, respectively. A 0.08 cm^2 or 1.0 cm^2 non-reflective mask was used to define the accurate active cell area. Incident photo-to-electron conversion efficiency (IPCE) spectra measurements were characterized using monochromatic incident light of 1×10^{16} photons cm^{-2} with the alternating current mode. All the tested cells in photovoltaic measurements were covered with a 0.08 cm^2 shading mask. Time-of-flight secondary ion mass spectrometry (ToF-SIMS) measurements were based on the focused ion beam ToF-SIMS spectrometer (ION TOF ToF SIMS 5-100). A Bi^+ ion beam was used as the ion beam to peel the samples. Dark *J-V* curves and EIS measurements were measured using a multi-functional electrochemical analysis instrument (Zahner, Germany).

Device stability measurement.

The operational stability tests were carried out at the MPP for the encapsulated devices under AM1.5 illumination (100 mW cm^{-2}). The devices were tested in BIR-50 solar cell light resistance testing system. During the aging test, the temperature of the light aging chamber was set at 85 °C. The devices were encapsulated in a nitrogen glove box. UV-curable epoxy was coated around the device area, and a customized glass cover slide with desiccant was attached to enclose the area.

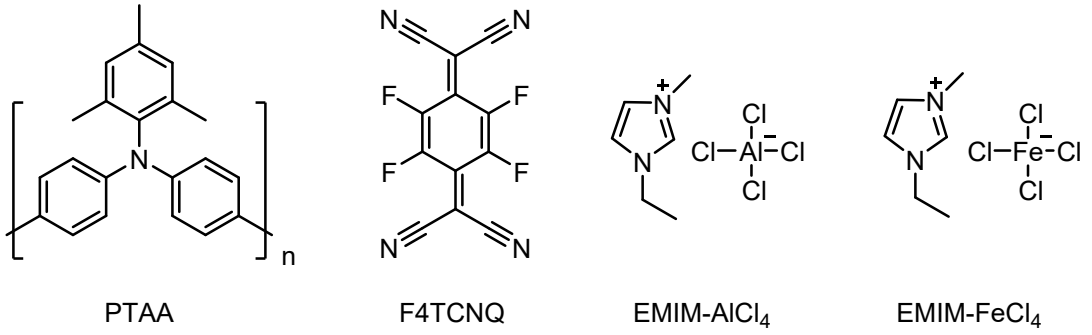

Figure S1. The chemical structures of PTAA, F4TCNQ, EMIM-$AlCl_4$, and EMIM-$FeCl_4$.

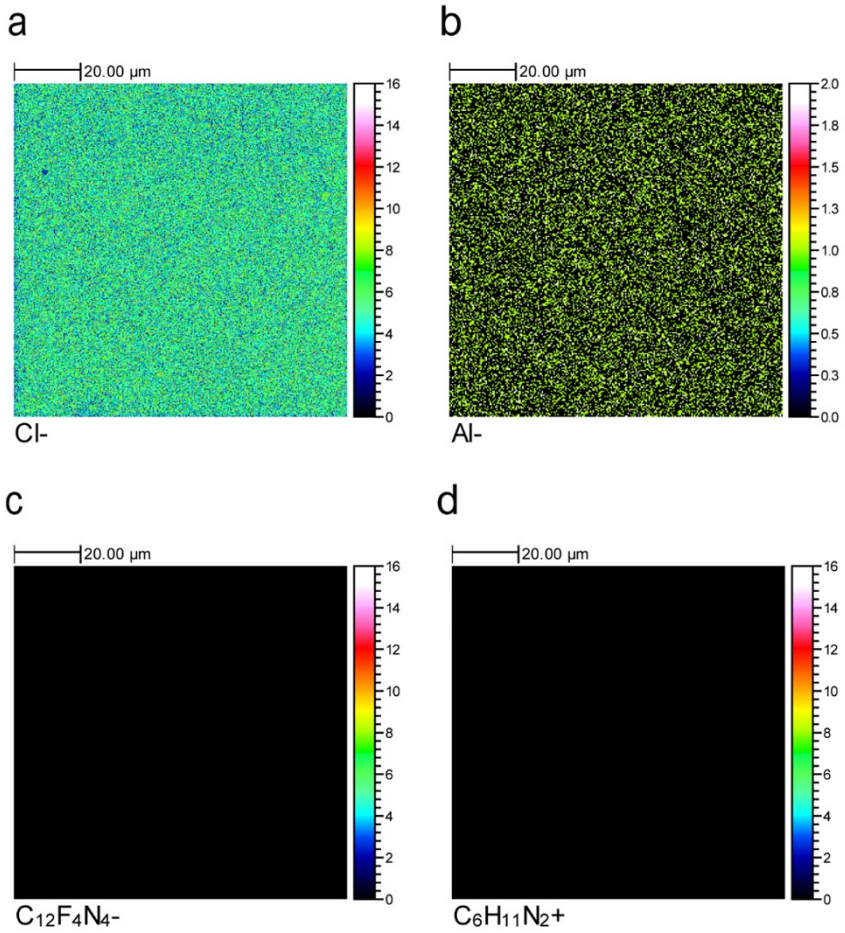

Figure S2. Mapping images of TOF-SIMS signals of (a) Cl^-, (b) Al^-, (c) $F4TCNQ^-$, and (d) $EMIM^+$ ions at the surface of $AlCl_4$-PTAA.

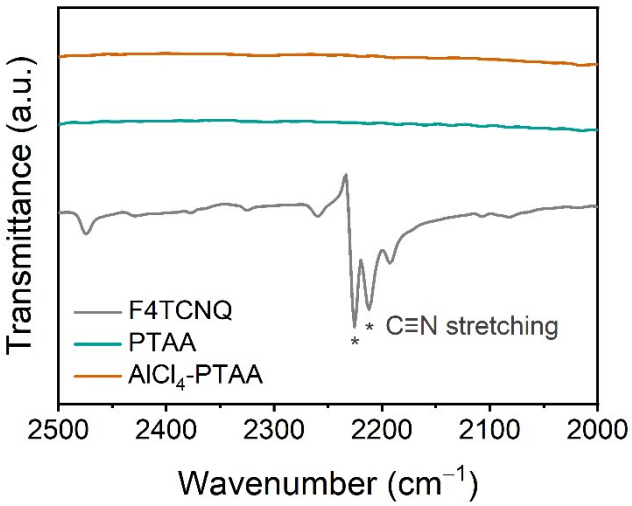

Figure S3. FTIR spectra of F4TCNQ, the pristine PTAA, and $AlCl_4$-PTAA at the range of 2,000-2,500 cm^{-1} to assess residual $F4TCNQ^{\bullet-}$ radical anions in anion-inserted PTAA thin films.

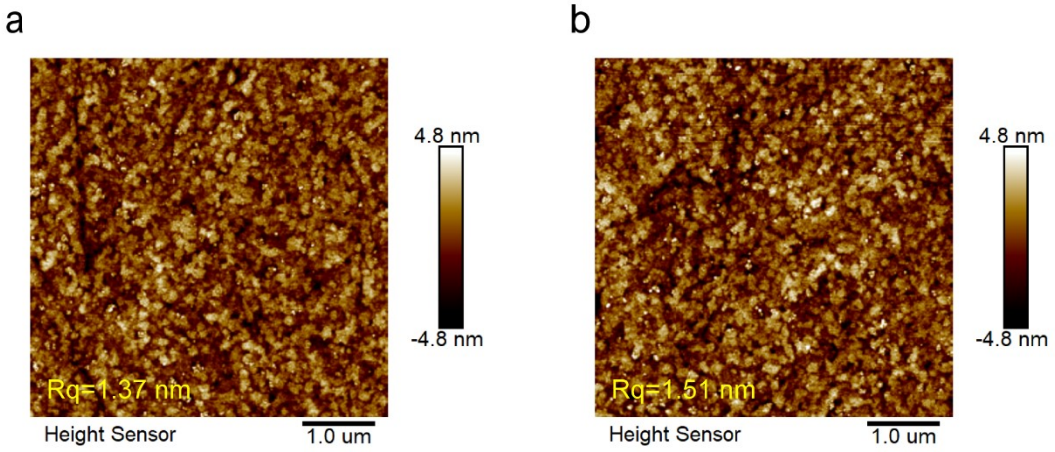

Figure S4. AFM height images of (a) the pristine PTAA, and (b) $AlCl_4$-PTAA.

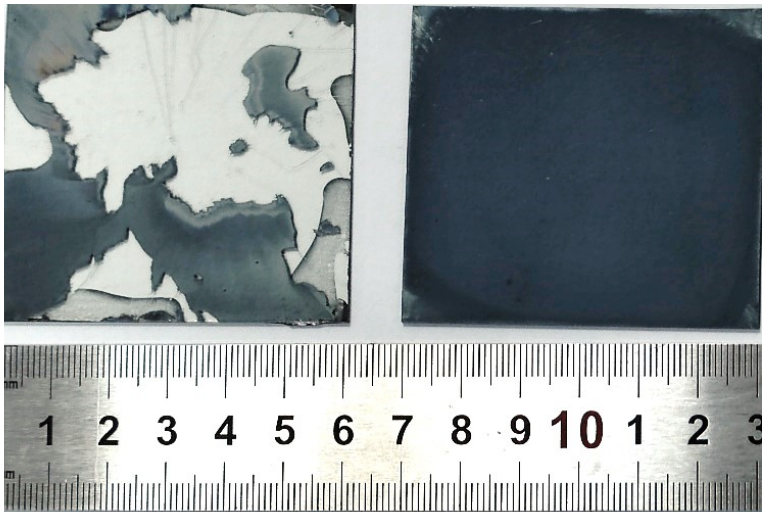

Figure S5. Photographs of perovskite films spin-coated on the pristine PTAA (left) and $AlCl_4$-PTAA (right) substrates. The substrate size is 60 mm × 60 mm.

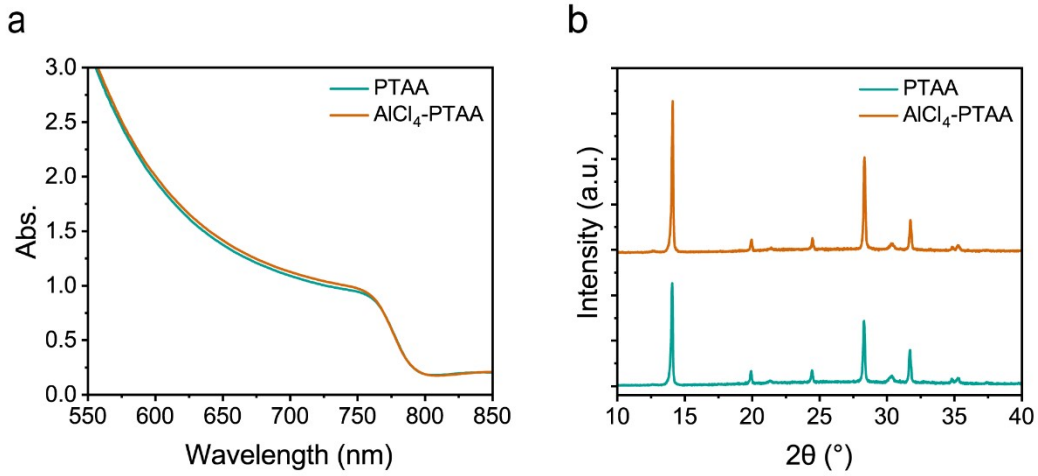

Figure S6. (a) Optical absorbance spectra and (b) X-ray diffraction patterns (XRD) of perovskite films deposited on the pristine PTAA and $AlCl_4$-PTAA substrates.

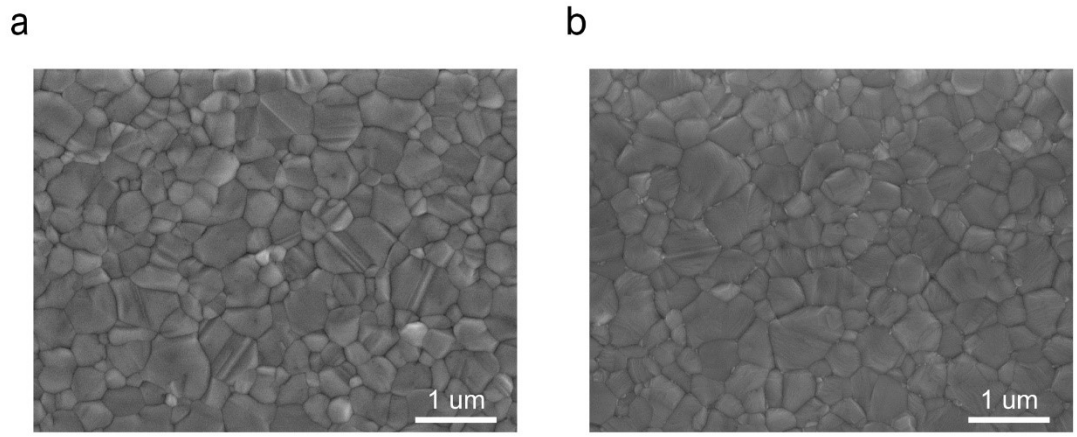

Figure S7. Scanning electron microscopy (SEM) images of perovskite films deposited on (a) the pristine PTAA, and (b) $AlCl_4$-PTAA substrates.

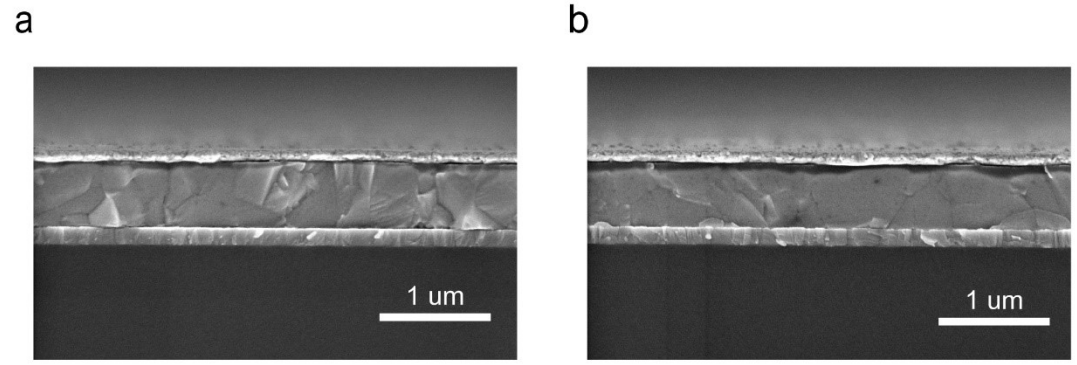

Figure S8. Cross-sectional SEM images of p-i-n PSCs fabricated with (a) the pristine PTAA, and (b) $AlCl_4$-PTAA.

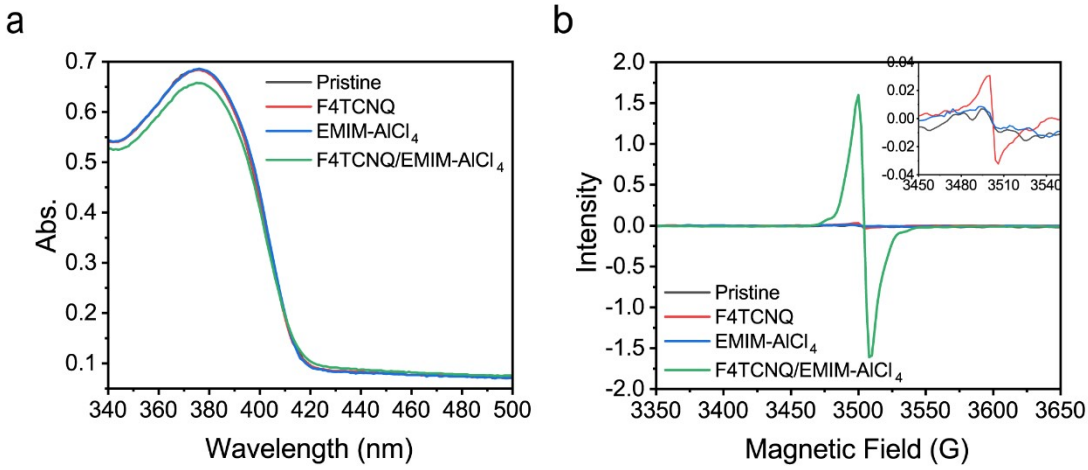

Figure S9. (a) Optical absorption spectra (b) ESR spectra of the pristine and doped PTAA layers after immersing in F4TCNQ or EMIM-$AlCl_4$ or F4TCNQ/EMIM-$AlCl_4$ solution in acetonitrile for 2 min and washing with fresh acetonitrile.

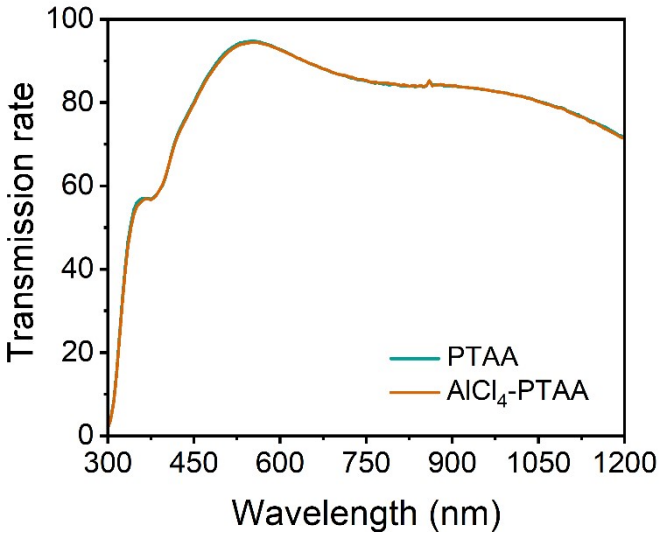

Figure S10. Transmittance spectra of the pristine PTAA and $AlCl_4$-PTAA thin films on ITO. It should be noted that PTAA thin films in transmittance spectra were fabricated by spin-coating 2 mg/ml PTAA solution at a spin speed of 6000 r.p.m, while the films in UV-vis spectra were fabricated by spin-coating 20 mg/ml PTAA solution at 3000 r.p.m.

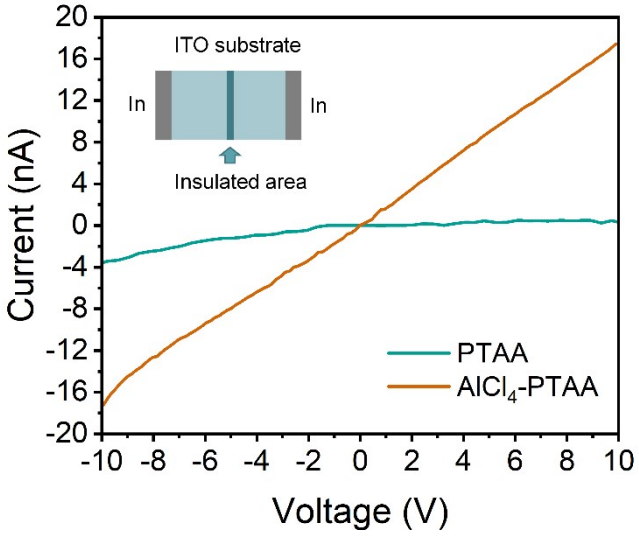

Figure S11. The Current-Voltage curves of the pristine PTAA and $AlCl_4$-PTAA. The inset is the design pattern for the measurement.

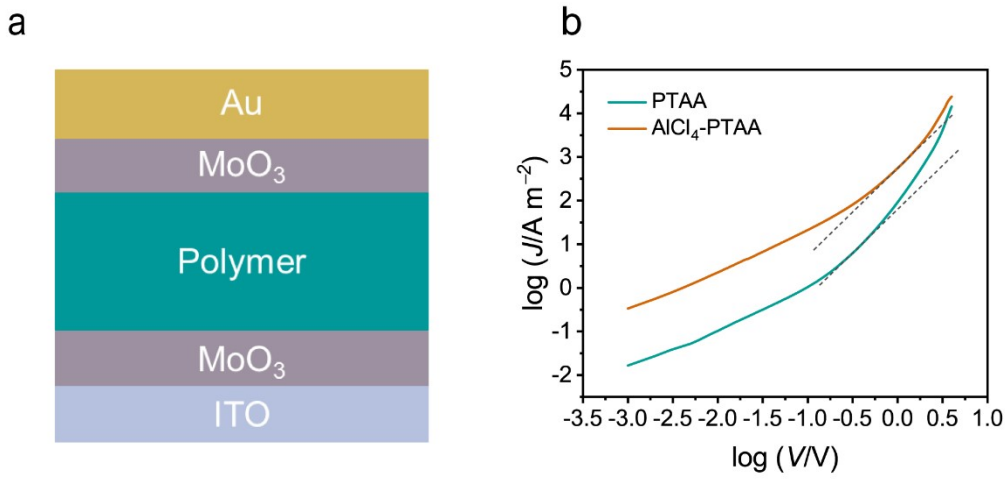

Figure S12. (a) Schematic device architectures of the hole-only device for SCLC measurement. (b) log(*J*)–log(*V*) plots for the devices based on the pristine PTAA and $AlCl_4$-PTAA.

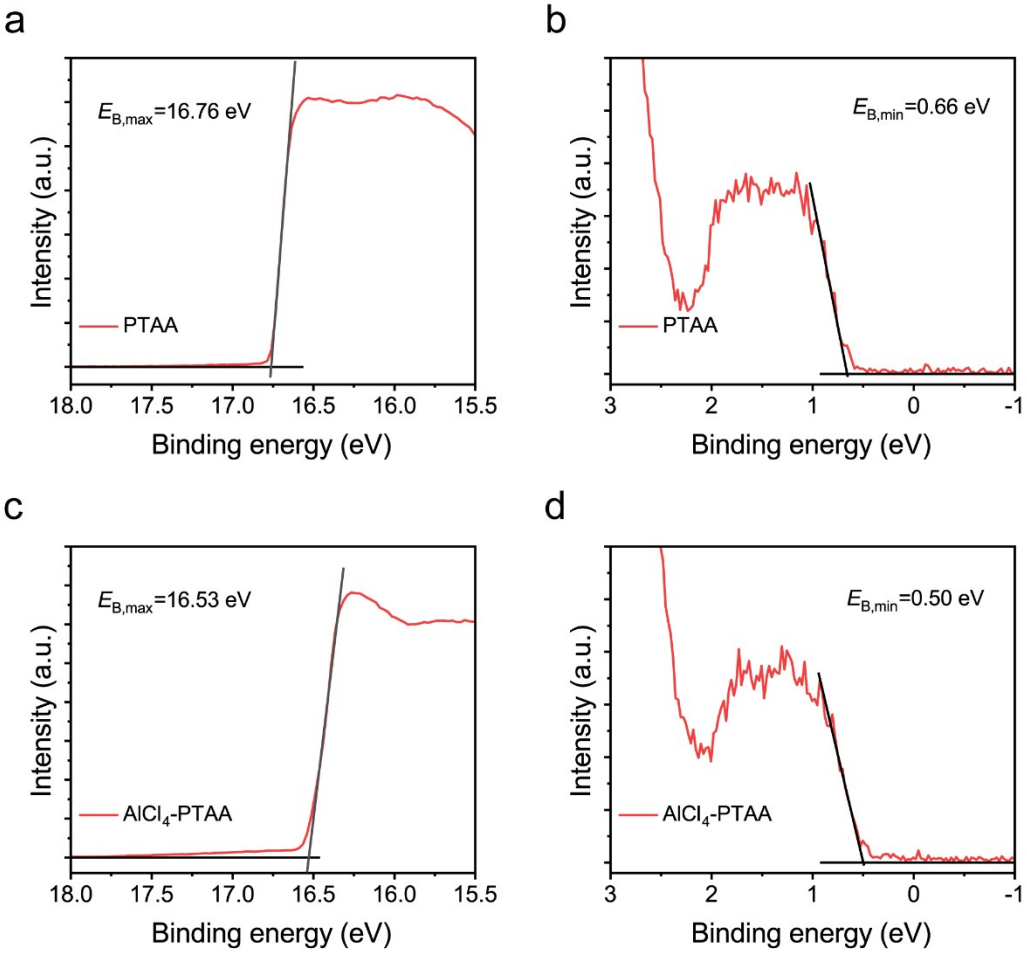

Figure S13. (a,c) The high-binding-energy and (b,d) the low-binding-energy cutoffs in UPS spectra of the pristine PTAA and $AlCl_4$-PTAA, respectively.

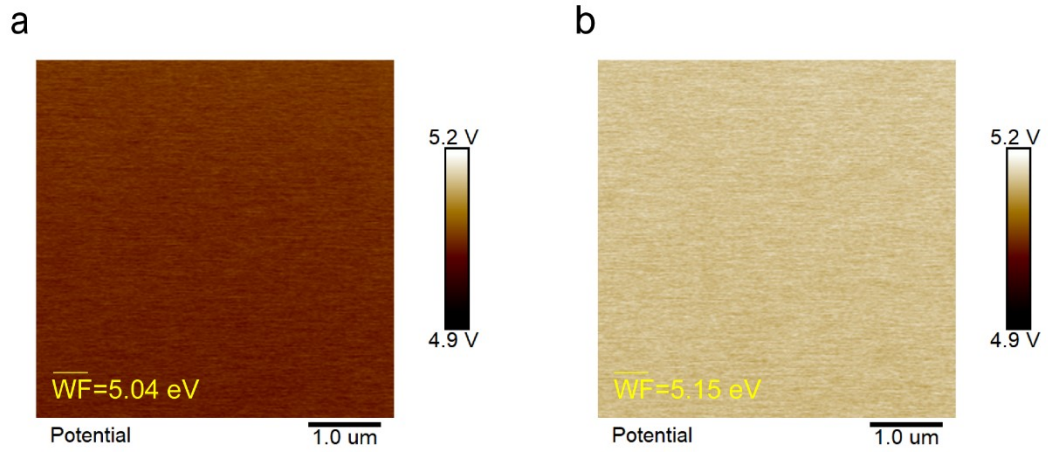

Figure S14. The x–y plane work function mapping images of (a) the pristine PTAA and (b) $AlCl_4$-PTAA. The surface work function (WF) had been calibrated by Au foil.

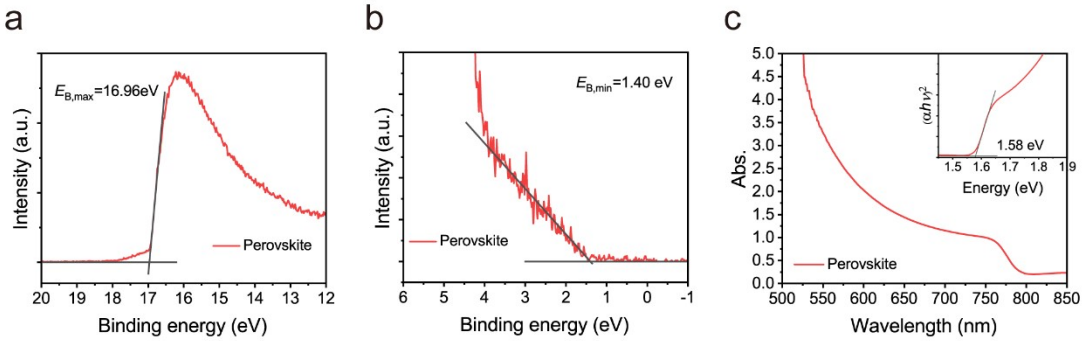

Figure S15. (a) The high-binding-energy, (b) the low-binding-energy cutoffs in UPS spectra, and (c) the UV-Vis spectrum of the perovskite film.

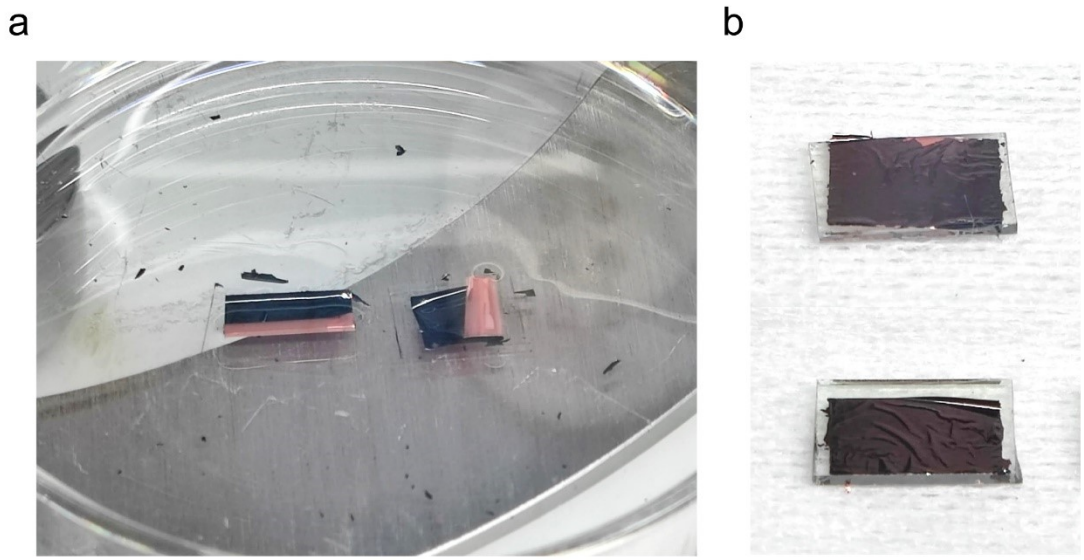

Figure S16. (a) Samples with the architecture of ITO/PTAA or $AlCl_4$-PTAA/Perovskite/Cu immersed in chlorobenzene solvent. The integrated perovskite/metal films had been detached from the substrates. The size of the substrate was reduced to 6 mm × 9 mm. One reason is to reduce the soaking time. Another reason is to ensure that the perovskite thin film of the PTAA sample was fully covered. (b) Prepared samples with the bottom sides up for the measurements on buried interfaces.

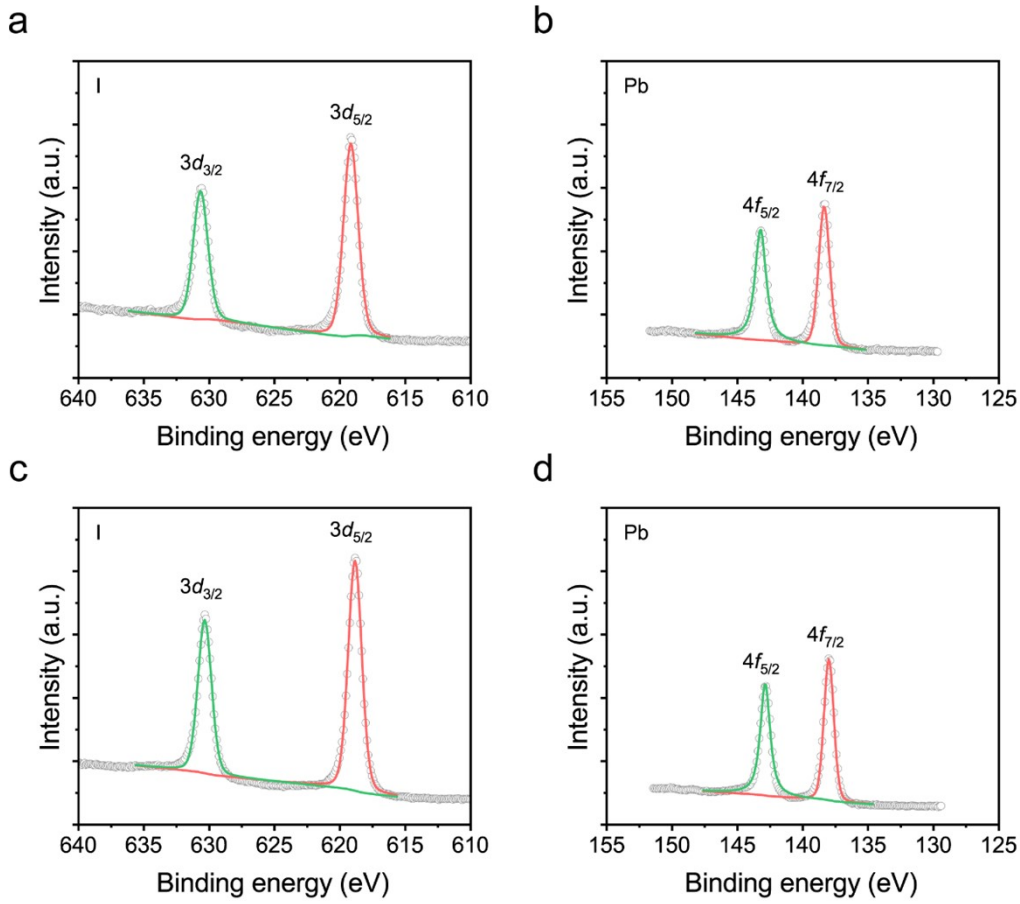

Figure S17. High-resolution XPS spectra of (a) I 3*d* and (b) Pb 4*f* for the bottom side of the $(CsPbI_3)_{0.05}[(FAPbI_3)_{0.92}(MAPbBr_3)_{0.08}]_{0.95}$ perovskite film on PTAA. The I/Pb ratio is 1.81 calculated from the fitting results, with respect to the nominal value of 2.77. (c) I 3*d* and (d) Pb 4*f* for the bottom side of the perovskite film on $AlCl_4$-PTAA. The I/Pb ratio is 2.25 calculated from the fitting results.

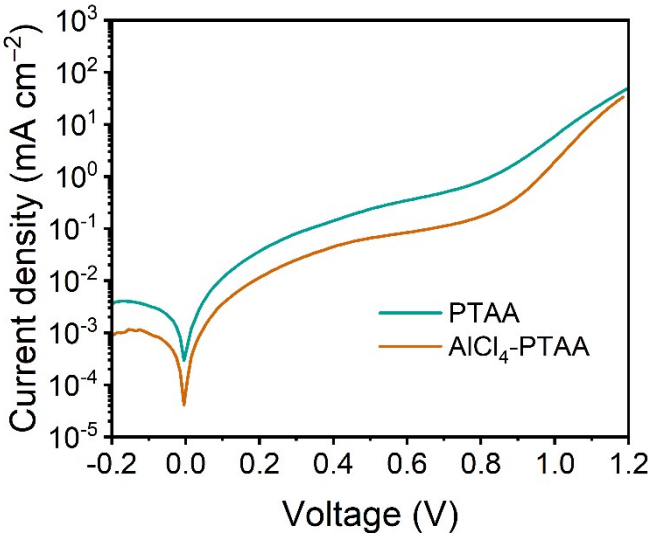

Figure S18. Dark *J-V* curves of the pristine PTAA and $AlCl_4$-PTAA based devices.

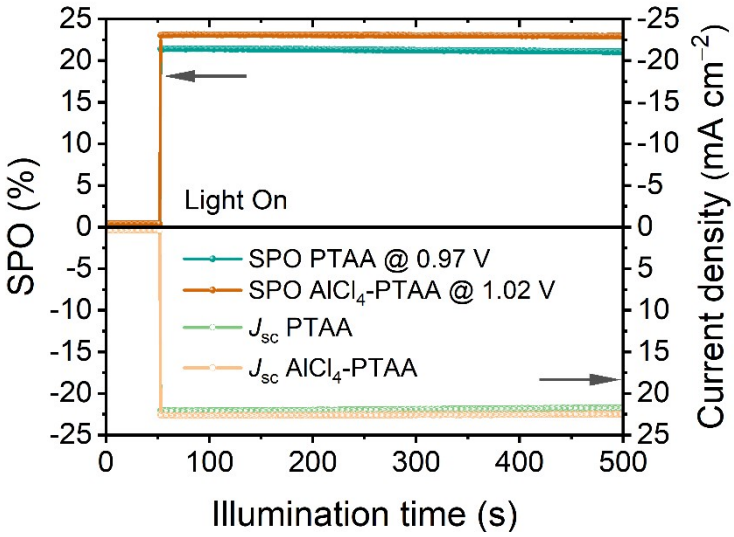

Figure S19. The stabilized power output (SPO) and photocurrent of the champion devices with the pristine PTAA and $AlCl_4$-PTAA at MPP voltage of 0.97 and 1.02 V, respectively.

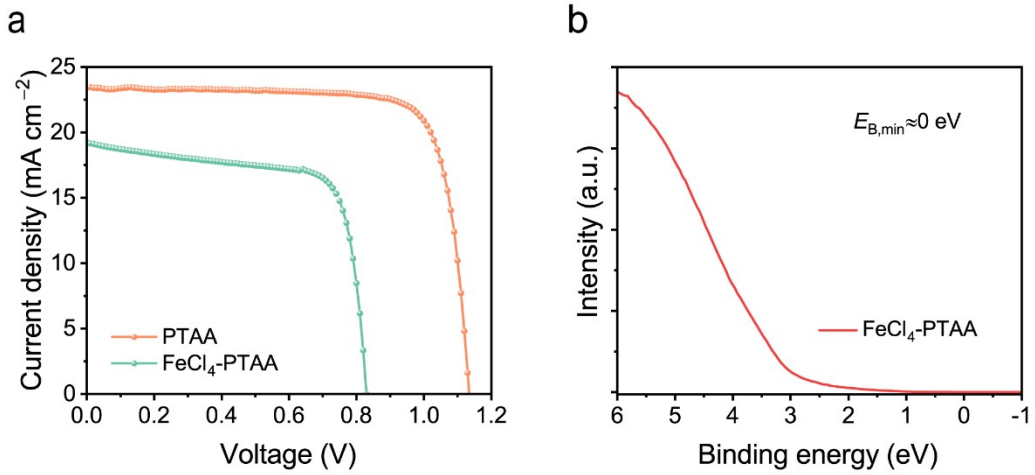

Figure S20. (a) *J-V* characteristics of p-i-n devices with the pristine PTAA and $FeCl_4$-PTAA. (b) The low-binding-energy cutoffs in UPS spectra of $FeCl_4$-PTAA.

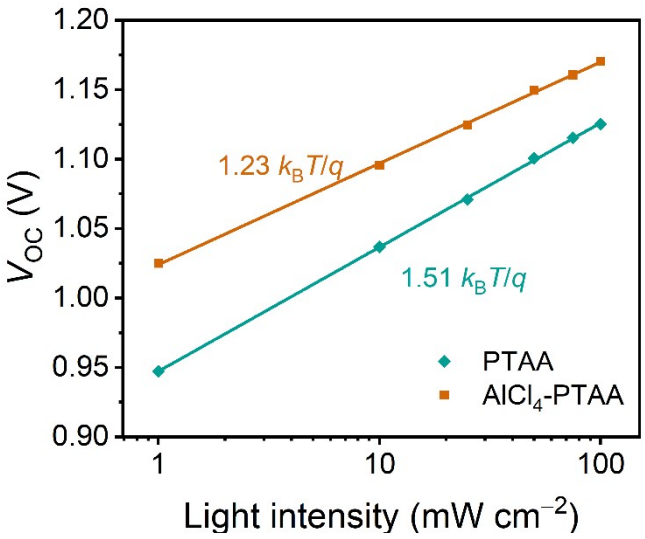

Figure S21. Light intensity-dependent V_{OC} for the devices with the pristine PTAA and $AlCl_4$-PTAA.

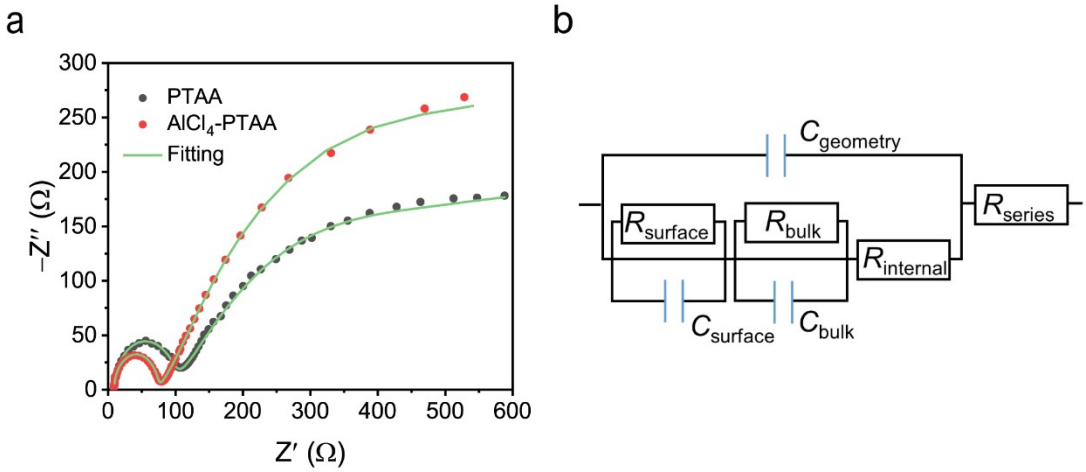

Figure S22. (a) Nyquist plots of PSCs with the pristine PTAA and $AlCl_4$-PTAA, measured under 1 sun illumination with a bias of 0.8 V. (b) The equivalent circuit for impedance spectroscopy fitting[6].

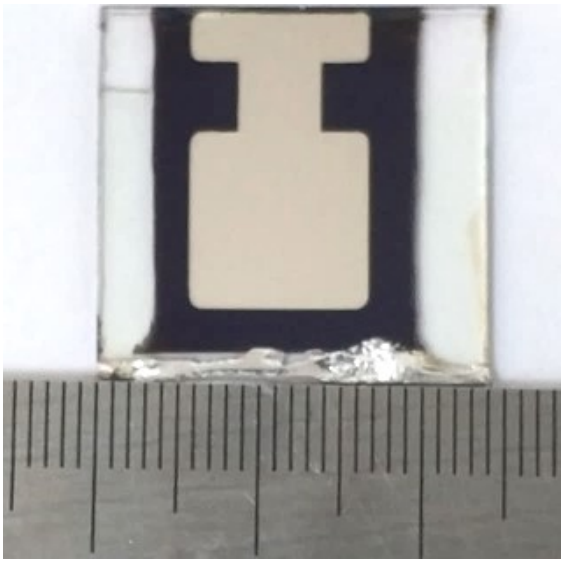

Figure S23. The photograph of the large-area $AlCl_4$-PTAA based device.

Table S1. The average conductivity of pristine PTAA and $AlCl_4$-PTAA.

Ion pairs	Average Conductivity (S cm^{-1})
PTAA	1.81×10^{-8}
$AlCl_4$-PTAA	6.52×10^{-7}

Table S2. The average hole mobility of pristine PTAA and $AlCl_4$-PTAA.

Ion pairs	Hole mobility (cm^2 $(Vs)^{-1}$)
PTAA	7.74×10^{-6}
$AlCl_4$-PTAA	6.70×10^{-5}

Table S3. PL decay lifetimes of perovskite films on different substrates. τ_1 and τ_2 correspond to the fast and slow decay components, respectively.

Films	τ_1	τ_2
Quartz/Perovskite	56	1741
PTAA/Perovskite	31	736
$AlCl_4$-PTAA/Perovskite	18	461

Table S4. The detailed parameters for the cells in Fig. 4a.

Devices	J_{SC} (mA cm^{-2})	V_{OC} (V)	FF (%)	PCE (%)
PTAA-Forward	23.75	1.127	80.88	21.65
PTAA-Reverse	23.65	1.132	79.66	21.33
$AlCl_4$-PTAA-Forward	24.02	1.177	81.92	23.16
$AlCl_4$-PTAA-Reverse	24.03	1.173	82.38	23.22

Table S5. The detailed parameters for the cells in Figure S21.

Devices	R_s (Ω)	$R_{surface}$ (Ω)	R_{bulk} (Ω)	$R_{internal}$ (Ω)
PTAA	9.721	179.5	4020	84.53
$AlCl_4$-PTAA	9.132	316.7	10039	63.56

Table S6. The detailed parameters for the cells in Fig. 4d.

Devices	J_{SC} (mA cm^{-2})	V_{OC} (V)	FF (%)	PCE (%)
1cm^2 PTAA	18.50	1.075	45.67	9.08
1cm^2 $AlCl_4$-PTAA	23.79	1.170	76.56	21.31

Table S7. Summary of the PTAA based p-i-n PSCs with the aperture area of around 1 cm^2.

Cell structure	PCE (%)	Area (cm^2)	Year	Reference
PTAA/Perovskite/PS/C_{60}/BCP/Cu	18.9	1.0	2017	(7)
PTAA/PFN-P2/Perovskite/LiF/C_{60}/BCP/Cu	20.3	1.0	2018	(8)
PTAA/Perovskite-DPSI/PCBM/C_{60}/BCP/Cu	18.3	1.0	2018	(9)
PTAA/PSBMA/Perovskite/PCBM/PSBMA/Al	15.72	1.0	2019	(10)
PTAA/Perovskite-BAA/C_{60}/BCP/Cu	20.0	1.1	2019	(11)

PTAA/CPE/Perovskite/LiF/C_{60}/Ag	18.38	1.0	2020	(12)
PTAA/Perovskite-TAH/PCBM/BCP/Ag	21.02	0.8	2020	(13)
PDMS/Li-TFSI/graphene/PTAA/Perovskite/ C_{60}/BCP/Ag	19.01	1.0	2021	(14)
PTAA/Perovskite (DMF/NMP)/C_{60}/BCP/Ag	21.2	1.0	2021	(15)
PTAA/Perovskite (evaporation)/C_{60}/BCP/Ag	18.1	1.0	2021	(16)
3Me-PTAA/Perovskite/PCBM/BCP/Ag	17.88	1.0	2022	(17)
$AlCl_4$-PTAA/Perovskite/PCBM/BCP/Ag	**21.31**	**1.0**	**2022**	**This work**

References

1. Y. Yamashita, J. Tsurumi, M. Ohno, R. Fujimoto, S. Kumagai, T. Kurosawa, T. Okamoto, J. Takeya and S. Watanabe, *Nature*, 2019, **572**, 634-638.
2. X. Zheng, Y. Hou, C. Bao, J. Yin, F. Yuan, Z. Huang, K. Song, J. Liu, J. Troughton, N. Gasparini, C. Zhou, Y. Lin, D.-J. Xue, B. Chen, A. K. Johnston, N. Wei, M. N. Hedhili, M. Wei, A. Y. Alsalloum, P. Maity, B. Turedi, C. Yang, D. Baran, T. D. Anthopoulos, Y. Han, Z.-H. Lu, O. F. Mohammed, F. Gao, E. H. Sargent and O. M. Bakr, *Nat. Energy*, 2020, **5**, 131-140.
3. A. Intaniwet, C. A. Mills, M. Shkunov, H. Thiem, J. L. Keddie and P. J. Sellin, *J. Appl. Phys.*, 2009, **106**, 064513.
4. X. Yang, D. Luo, Y. Xiang, L. Zhao, M. Anaya, Y. Shen, J. Wu, W. Yang, Y.-H. Chiang, Y. Tu, R. Su, Q. Hu, H. Yu, G. Shao, W. Huang, T. P. Russell, Q. Gong, S. D. Stranks, W. Zhang and R. Zhu, *Adv. Mater.*, 2021, **33**, 2006435.
5. Y. Chen, Z. Yang, S. Wang, X. Zheng, Y. Wu, N. Yuan, W.-H. Zhang and S. Liu, *Adv. Mater.*, 2018, **30**, 1805660.
6. Y. Shao, Z. Xiao, C. Bi, Y. Yuan and J. Huang, *Nat. Commun.*, 2014, **5**, 5784-5784.
7. M. Stolterfoht, C. M. Wolff, Y. Amir, A. Paulke, L. Perdigón-Toro, P. Caprioglio and D. Neher, *Energy Environ. Sci.*, 2017, **10**, 1530-1539.
8. M. Stolterfoht, C. M. Wolff, J. A. Márquez, S. Zhang, C. J. Hages, D. Rothhardt, S. Albrecht, P. L. Burn, P. Meredith, T. Unold and D. Neher, *Nat. Energy*, 2018, **3**, 847-854.
9. X. Zheng, Y. Deng, B. Chen, H. Wei, X. Xiao, Y. Fang, Y. Lin, Z. Yu, Y. Liu, Q. Wang and J. Huang, *Adv. Mater.*, 2018, **30**, 1803428.
10. Q. Chen, L. Yuan, R. Duan, P. Huang, J. Fu, H. Ma, X. Wang, Y. Zhou and B. Song, *Sol. RRL*, 2019, **3**, 1900118.
11. W.-Q. Wu, Z. Yang, P. N. Rudd, Y. Shao, X. Dai, H. Wei, J. Zhao, Y. Fang, Q. Wang, Y. Liu, Y. Deng, X. Xiao, Y. Feng and J. Huang, *Sci. Adv.*, 2019, **5**, eaav8925.
12. E. D. Jung, A. K. Harit, D. H. Kim, C. H. Jang, J. H. Park, S. Cho, M. H. Song

and H. Y. Woo, *Adv. Mater.*, 2020, **32**, 2002333.
13. K. Liu, Q. Liang, M. Qin, D. Shen, H. Yin, Z. Ren, Y. Zhang, H. Zhang, P. W. K. Fong, Z. Wu, J. Huang, J. Hao, Z. Zheng, S. K. So, C.-S. Lee, X. Lu and G. Li, *Joule*, 2020, **4**, 2404-2425.
14. J. H. Heo, D. S. Lee, F. Zhang, C. Xiao, S. J. Heo, H. J. Lee, K. Zhu and S. H. Im, *Sol. RRL*, 2021, **5**, 2100733.
15. F. H. Isikgor, A. S. Subbiah, M. K. Eswaran, C. T. Howells, A. Babayigit, M. De Bastiani, E. Yengel, J. Liu, F. Furlan, G. T. Harrison, S. Zhumagali, J. I. Khan, F. Laquai, T. D. Anthopoulos, I. McCulloch, U. Schwingenschlögl and S. De Wolf, *Nano Energy*, 2021, **81**, 105633.
16. M. M. Tavakoli and R. Tavakoli, *Phys. Status Solidi RRL*, 2021, **15**, 2000449.
17. C. Wang, Q. Xiong, Z. Zhang, L. Meng, F. Li, L. Yang, X. Wang, Q. Zhou, W. Fan, L. Liang, S.-Y. Lien, X. Li, J. Wu and P. Gao, *ACS Appl. Mater. Interfaces*, 2022, **14**, 12640-12651.